Mineralium Deposita
https://doi.org/10.1007/s00126-020-00955-z

ARTICLE

High-sulfidation veins in the Jiama porphyry system, South Tibet

Shi-Ji Zheng[1,2] · Hong Zhong[1,2] · Zhong-Jie Bai[1] · Zhong-Kun Zhang[3] · Cheng-Quan Wu[1]

Received: 24 August 2019 / Accepted: 6 January 2020

Abstract

The giant Jiama polymetallic ore deposit is a porphyry–skarn system in the eastern Gangdese porphyry belt of the Tibetan Plateau. Steeply dipping high-grade massive sulfide veins are classified as lode-type high-sulfidation (HS) mineralization comprising mainly Cu-sulfosalts in Au-poor and Au-rich veins. Au-poor veins contain an As-rich pyrite–enargite–tennantite assemblage, whereas Au-rich veins contain an Sb-rich enargite–luzonite–tetrahedrite–chalcostibite–watanabeite assemblage. The coexistence of pyrite, dendritic muscovite, and euhedral quartz in the Cu-sulfosalts indicates slightly acidic or near-neutral formation conditions. Most Au- and Ag-bearing minerals are inclusions of tellurides (hessite, sylvanite, and petzite) in tennantite–tetrahedrite, and watanabeite. Au and Ag concentrations in tennantite–tetrahedrite, watanabeite, and chalcostibite are much higher than in enargite and luzonite, confirming that they were controlled by intermediate-sulfidation state Cu–As–Sb–S solid solutions, with Au tending to be enriched in Sb-rich minerals compared with As-rich solid solutions. The HS veins overlying the known porphyry intrusion and cutting skarn orebodies in the Jiama deposit constitute a porphyry–skarn–high sulfidation system. The occurrence of HS veins suggests that channels in paleo-fumaroles and the mineralization that resulted may be ascribed to expansion of magmatic vapor. HS veins close to the porphyry intrusion exposed at the surface indicate that shallow epithermal disseminated mineralization was likely removed by rapid regional uplift and erosion of the Gangdese porphyry belt.

Keywords HS veins · Jiama porphyry system · Gold and silver · Uplift and erosion

Introduction

Porphyry deposits and related skarn and high-sulfidation (HS) epithermal deposits are commonly distributed at the convergent plate margins of great crustal thickness, with the most representative being the Andean and Tethyan metallogenic belts (Sillitoe and Perelló 2005; Chiaradia 2014; Lee 2014; Sun et al. 2017).

Sillitoe (2010) proposed a model of porphyry Cu systems comprising porphyry–skarn–HS deposits (proximal Cu–Au skarn and distal Pb–Zn skarn, upper HS high-grade massive sulfide lodes, and near-surface high-tonnage disseminated epithermal orebodies). The coexistence of all three types in one deposit is rare (e.g., Recsk mine, Hungary; Molnár et al. 2008; Takács et al. 2017), as it requires optimal combinations of a series of geological conditions, including the presence of carbonate host rocks for skarn formation. Subsurface HS epithermal deposits are not easily preserved owing to exhumation by uplift and erosion (Taylor 2007), especially in plateau regions. The Andean Cu province is associated with subduction and hosts many major porphyry, porphyry-related skarn, and HS deposits (Sillitoe and Perelló 2005). The HS deposits are Oligocene to Miocene in age and crop out at > 3500 m above sea level (a.s.l.) (e.g., the El Indio and Maricunga belts in the Southern Andes; Muntean and Einaudi 2001; Bissig et al. 2002, 2015). Tethyan orogens associated with both subduction and collision also include HS epithermal deposits in high-altitude regions, such as the ca. 90 Ma Chelopech (Bulgaria; Chambefort et al. 2007) and ca. 30 Ma Perama Hill (Greece; Voudouris et al. 2011) deposits. The Tibetan Plateau, part of the eastern Tethyan segment, also contains several porphyry belts, including the Yulong, Bangonghu–

Editorial handling: K. Kelley

Electronic supplementary material The online version of this article (https://doi.org/10.1007/s00126-020-00955-z) contains supplementary material, which is available to authorized users.

✉ Hong Zhong
zhonghong@vip.gyig.ac.cn

[1] State Key Laboratory of Ore Deposit Geochemistry, Institute of Geochemistry, Chinese Academy of Sciences, Guiyang 550081, China

[2] University of Chinese Academy of Sciences, Beijing 100049, China

[3] Tibet Huatailong Mining Development Co., Ltd, China National Gold Group, Lhasa 850200, China

Published online: 18 January 2020

Nujiang, and Gangdese belts (Fig. 1a; Hou et al. 2011). Giant HS epithermal deposits in the Cretaceous Bangonghu–Nujiang belt, typified by the Duolong ore district (Cu resource > 20 Mt, > 4000 m a.s.l), have been documented in recent years (Tang et al. 2014; Li et al. 2015). The Gangdese porphyry belt has similar elevation, geochemical characteristics, and metallogenic evolution as the Andean porphyry-HS belt (Hou et al. 2011; Richards 2015). Low-sulfidation epithermal deposits such as the ca. 60 Ma Sinongduo Ag–Pb–Zn deposit (Li et al. 2019) have recently been documented, but no HS deposits have previously been reported in the Gangdese belt. Here, we provide the first report of detailed geological, mineralogical, and geochemical investigations of lode-type HS mineralization in the Jiama giant porphyry–skarn deposit. The genesis of Au and Ag in the HS mineralization is also discussed.

General geology

The Gangdese porphyry Cu belt is located in the Lhasa Terrane, which is bounded by the Indus-Yarlung suture to the south and the Bangong-Nujiang suture to the north, and contains some of the most prospective Cu–polymetallic prospects in China. The belt lies parallel to the Indian-Asian collisional zone and extends E to W for several hundred kilometers (Qu 2001; Qu et al. 2004; Fig. 1a). Three episodes of porphyry formation in the belt are associated with Indian-Asian continental collision: Paleocene-Eocene (e.g., the Yaguila and Sharang deposits), Oligocene (e.g., the Zedang and Nuri deposits), and Miocene; these episodes are related to the main collisional convergent setting, a late collisional transformation setting, and a post-collisional extension setting, respectively (Hou 2010; Wang et al. 2014; Hu et al. 2015). The Miocene porphyry deposits (of greatest economic value) formed primarily in the older Gangdese granite batholith in a narrow belt parallel to the Indian-Asian collisional zone. These include the giant Qulong (10.6 Mt Cu; Hu et al. 2015) and Jiama deposits and several medium- to large-sized deposits including the Tinggong, Bangpu, Lakang'e, Nanmu, and Chongjiang deposits (Wang et al. 2014; Sun et al. 2018).

The Jiama deposit contains at least 7.4 Mt Cu (grading 0.39%), 0.6 Mt Mo (0.03%), 1.1 Mt Pb (0.06%), 0.7 Mt Zn (0.04%), 360.3 Moz Ag (5.92 g t^{-1}), and 6.7 Moz Au (0.11 g t^{-1}) and consists of Cu–Mo porphyry, Cu–polymetallic skarns (Cu-Ag-Au and Cu-Pb-Zn skarn), and Cu–Mo hornfels (Tang et al. 2010, 2011; Zheng et al. 2016; Fig. 1b, c). The Jiama deposit is the second largest deposit in the Gangdese belt, second only to the adjacent Qulong deposit, but it is economically more important in the Gangdese porphyry belt with its high-grade polymetallic resources. The porphyry Cu–Mo zones that are situated at < ~4600 m a.s.l host disseminated and quartz-veinlet chalcopyrite and molybdenite. The ore-related porphyries include granite porphyry, quartz-diorite porphyry, and monzonitic granite

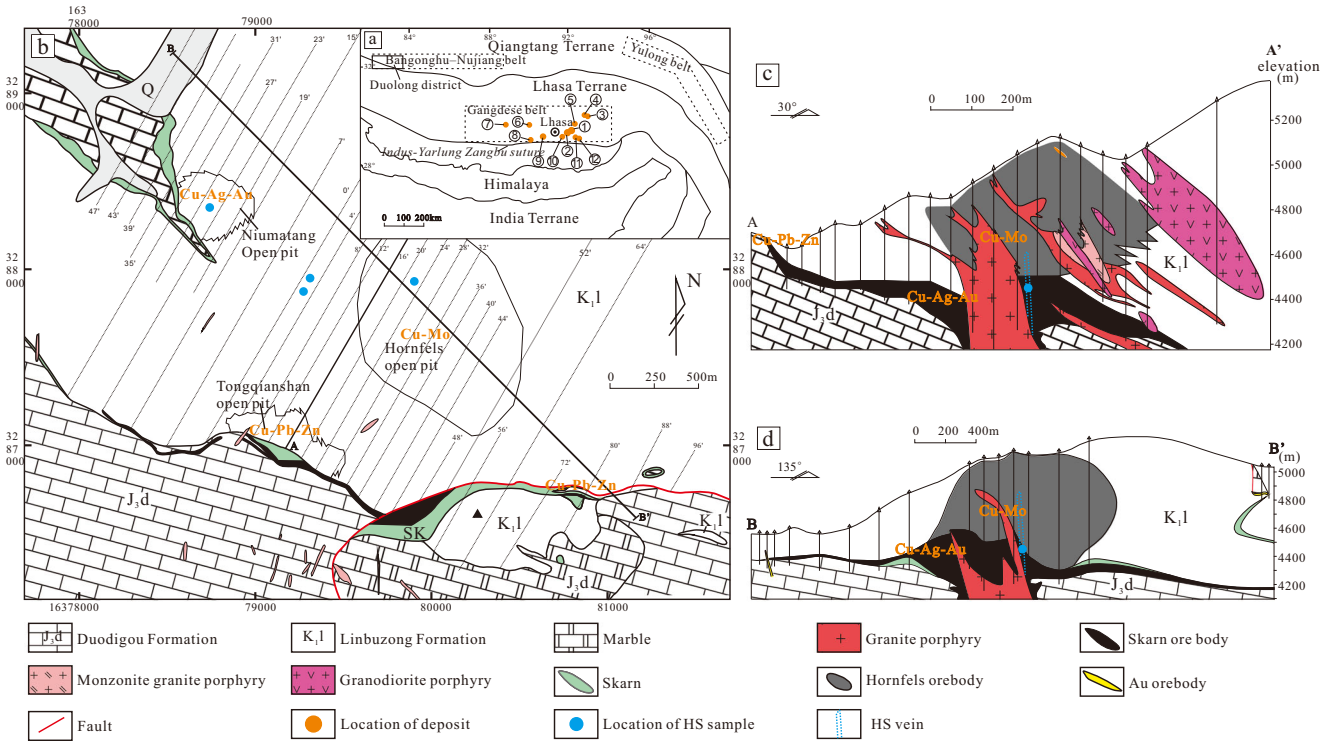

Fig. 1 **a** Tectonic and location map of the Gangdese porphyry Cu belt in Southern Tibet (1 Jiama, 2 Qulong, 3 Yaguila, 4 Sharang, 5 Bangpu, 6 Tinggong, 7 Sinongduo, 8 Chongjiang, 9 Nanmu, 10 Lakang'e, 11 Nuri, 12 Zedang). **b** Simplified geological map of the Jiama mine. **c**, **d** Geological cross-sections A–A' and B–B' (modified after Tang et al. 2010, 2013)

porphyry, which are mostly of calc-alkaline to high-K calc-alkaline series (Tang et al. 2013). Associated hydrothermal alteration includes potassic alteration at the center of intrusions, zoning outwards to chlorite-sericite-pyrite and distal propylitic, and later superimposed argillic alteration (Zheng et al. 2016). The most economically important skarn Cu–polymetallic orebodies occur at elevations of 3800–5300 m a.s.l., dominantly above porphyry intrusions and within the contact zones between carbonate sequences of the Jurassic Duodigou Formation (J_3d) and pelitic rocks of the Cretaceous Linbuzong Formation (K_1l) (Fig. 1c, d). The maximum thickness of skarn orebodies is > 200 m. The skarn minerals include calcium garnet from andradite–grossular, wollastonite, and small amounts of pyroxene, epidote, and tremolite. Proximal oxidized-type Cu–Ag–Au skarns comprise primarily bornite, chalcopyrite, wittichenite, hessite, and electrum, and distal Cu-Pb–Zn (Ag) skarns have galena, sphalerite and chalcopyrite (Fig. 1c). Hornfels mineralization formed from contact between underlying porphyry intrusions and the Linbuzong Formation (Fig. 1c, d); hornfels zones occur at 4200–5300 m a.s.l. with a thickness of up to 1000 m; quartz-veinlet chalcopyrite and molybdenite in the hornfels zones are similar to porphyry zones (Wang et al. 2011; Wang and Tang 2011). The hornfels is considered part of the skarn mineralizing processes (Meinert 2000; Meinert et al. 2005).

This study focuses on the high-sulfidation Cu–Ag–Au massive sulfide veins. The veins occur in porphyry dikes and overprint skarn mineralization and are characterized by silicification and pyrite-sericite alteration. They were previously characterized as epigenetic or low-sulfidation epithermal deposits (Ren et al. 2002; Zheng et al. 2016), but our field studies indicate that these veins are fracture-controlled, and based on mineral assemblages, we infer they are high-sulfidation (HS) veins (Fig. 1). The scale of the HS veins is small compared with skarn orebodies, but they are widely distributed in the Jiama deposit and are found in both open pit walls and underground tunnels (Fig. 2a, b). The HS veins are mainly NE trending (20–40°) and steeply dipping, and they extend vertically and horizontally for tens to hundreds of meters with widths of a few centimeters to 50 cm at elevations of < 4420 m a.s.l. to the surface at > 4520 m a.s.l. Based on field relationships that indicate the HS veins cut skarn and hornfels, they formed relatively late (Fig. 2). Ore from these HS veins contains 30–90 vol.% Cu–As–Sb–S sulfosalt minerals, including primarily enargite–luzonite, watanabeite, tennantite–tetrahedrite, and chalcostibite. Euhedral quartz is the predominant ore-related gangue mineral associated with the sulfosalts, and both are extensively superimposed by later carbonate minerals (Fig. 2c). Minor realgar is common in the fracture zone at vein pinchouts (Fig. 2g). Hydrothermal brecciation also occurs in some veins (Fig. 2c). Differences in mineral assemblages and amount of gold permit classification as Au-poor or Au-rich HS veins. The Au-poor veins host an As-rich pyrite–enargite–tennantite mineral assemblage, whereas the Au-rich veins contain a mineral assemblage consisting of Sb-rich enargite, luzonite, tennantite, tetrahedrite, watanabeite, and chalcostibite. The Au-poor and Au-rich veins are analogous to the Cu and Au stages of the El Indio deposit (Jannas et al. 1990, 1999).

Analytical methods

Five finely powdered samples were completely dissolved by acid digestion method, and their chemical compositions were determined by inductively coupled plasma–mass spectrometry (ICP–MS) at ALS Chemex, Guangzhou, China. Chemical compositions of specific mineral phases in HS veins were derived by analyses using a JEOL JXA 8100 electron-probe microanalysis (EPMA) system at the State Key Laboratory for Mineral Deposits Research, Nanjing University, Nanjing, China, with operating conditions of 15 kV voltage, 20 nA beam current, and 3 μm beam diameter, with counting times of 5–20 s. Laser ablation-ICP-MS (LA-ICP-MS) analyses were conducted using a NewWave 213 nm LA system coupled to an Agilent 7700X Quadrupole ICP-MS instrument at the State Key Laboratory of Ore Deposit Geochemistry, Institute of Geochemistry, Chinese Academy of Sciences, Guiyang, China. The laser-beam energy flux was 3.5 mJ cm^{-2} with a beam diameter of 50 μm. The analysis time was 90 s, including 20 s background acquisition, and 70 s of sample data acquisition. The following isotopes were detected: ^{34}S, ^{55}Mn, ^{57}Fe, ^{59}Co, ^{60}Ni, ^{65}Cu, ^{66}Zn, ^{69}Ga, ^{72}Ge, ^{74}Ge, ^{75}As, ^{77}Se, ^{107}Ag, ^{111}Cd, ^{115}In, ^{118}Sn, ^{121}Sb, ^{125}Te, ^{182}W, ^{197}Au, ^{202}Hg, ^{205}Tl, ^{208}Pb, and ^{209}Bi. Data reduction involved LADR software (https://norsci.com), with Cu concentration values (EPMA) being used as an internal standard and standards GSE-1G and mass-1(PS-1) as external standards (Longerich and Sylvester 2008; Danyushevsky et al. 2011).

Mineralogy and chemical compositions

All five bulk ore samples contain significant concentrations of Cu (> 10%), S (> 8%), As > 2.2%), and Sb (2.1% to more than 20%) (Fig. 3a, Table A1), corresponding to their Cu–As–Sb–S mineral assemblages. Au-poor samples are characterized by As > Sb contents, Ag contents of 185 to 239 ppm, and Au contents below detection limit (< 0.05 ppm). Au-rich samples are Sb-rich compared with As, with 580 to 1100 ppm Ag, and 7 to 54 ppm Au. High Te contents (350 to 2320 ppm) in both Au-rich and Au-poor samples reflect the presence of Au or Ag telluride minerals. In general, the major- and trace-element contents of bulk samples indicate the presence of minerals such as enargite/luzonite, tennantite–tetrahedrite, watanabeite, and chalcostibite (Table A2, Fig. 3b). The time-resolved spectra from LA-ICP-MS analyses of enargite, luzonite, tennantite, and tetrahedrite are shown in Fig. A1. Mineral associations and their chemical variations are described below.

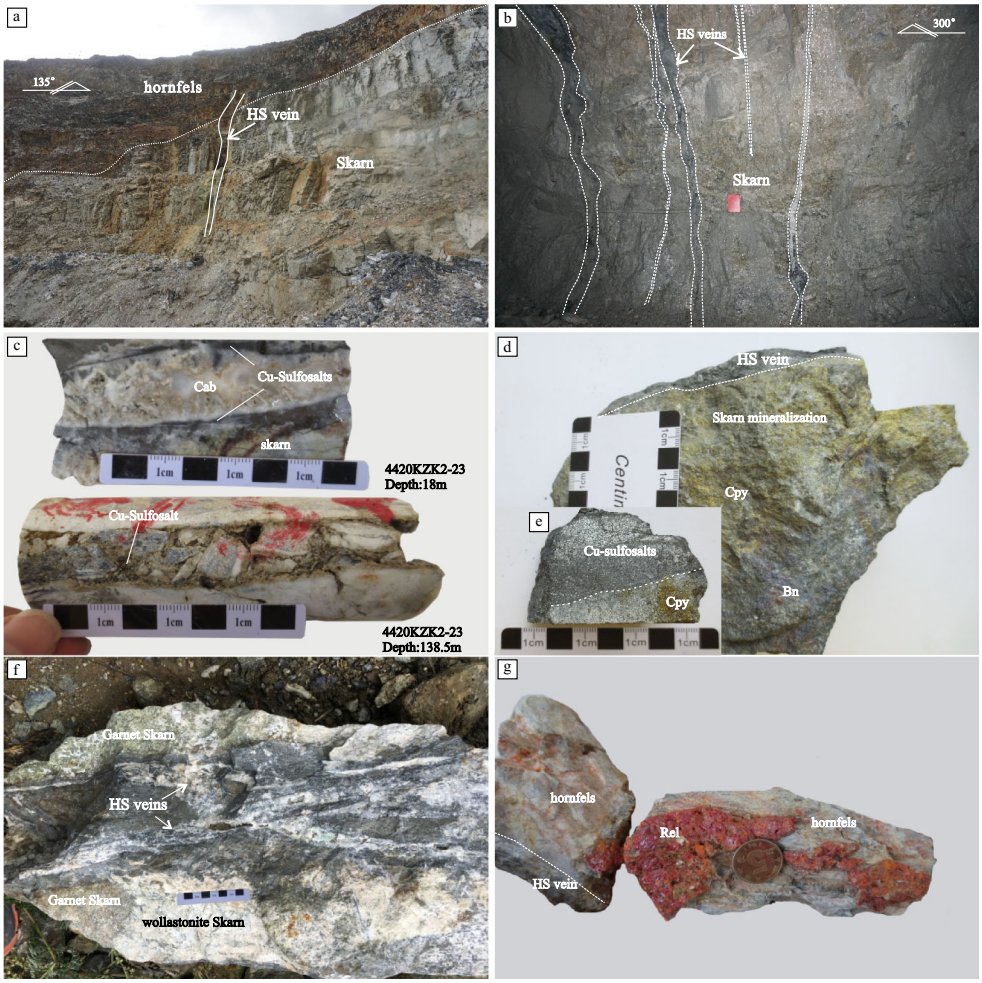

Fig. 2 **a** HS vein cutting skarn and hornfel in a section of the Niumatang open pit. **b** HS veins cutting skarn on the wall of tunnel at 4490 m a.s.l. **c** Core samples from drill hole of 4420KZK2-23 showing HS veins cutting skarn, marginal Cu-sulfosalts followed by carbonate minerals (Cab) at ~ 4400 m a.s.l., and brecciation after Cu-sulfosalt mineralization at ~ 4280 m a.s.l. **d**, **e** Massive HS mineralization cutting skarn mineralization, with chalcopyrite (Cpy) and bornite (Bn). **f** HS veins cutting garnet and wollastonite skarn. **g** HS vein cutting hornfels and realgar (Rel) on the surface of hornfels

Au-poor veins

Enargite, tennantite, and pyrite are the dominant sulfides in Au-poor veins, comprising at least 90 vol.% of total sulfides. Watanabeite, galena, melonite, chalcopyrite, hessite, and bournonite occur as inclusions in tennantite; scheelite and covellite occur in enargite (Fig. 4). Enargite is euhedral to subhedral or occurs as massive aggregates (Fig. 4a, b). Enargite contains up to 3.41 wt% Sb, and averages 110 ppm Ge, 108 ppm Se, 10.5 ppm Hg, and 9.90 ppm Ag (Table A2).

Tennantite commonly occurs as massive aggregates and host abundant mineral inclusions (Fig. 4c–f). Relatively, early enargite,

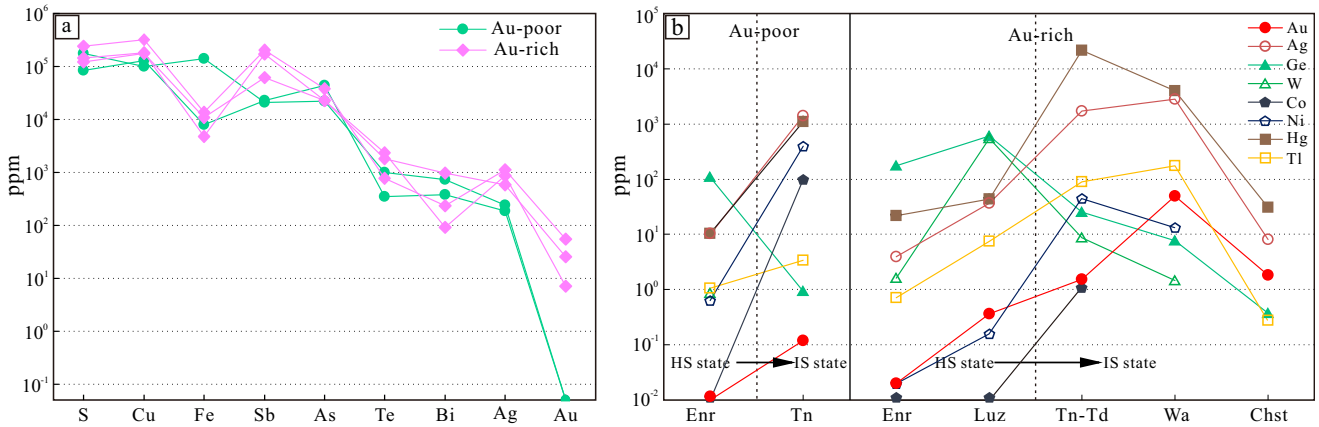

Fig. 3 **a** Contents of selected elements in ore samples from the HS veins. **b** Mean contents of selected trace elements in Cu-sulfosalts from Au-poor and Au-rich veins. Enr, enargite; Tn, tennnantite; Luz, luzonite; Tn-Td, tennantite-tetrahedrite; Wa, watanabeite; Chst, chalcostibite

pyrite, and euhedral quartz are partially dissolved by tennantite (Fig. 4b–i). Tennantites are ferroan (Fe content > 3.65 wt%) and Cu-excess tennantites (with Cu > 10 atoms per formula unit in the formula; Marcoux et al. 1994) that are common in HS epithermal deposits (e.g., Pefka deposit, Greece; Repstock et al. 2015). A wide variety of elements are enriched in Fe-tennantite (Table A2, Fig. A1), including Ag (up to 1891 ppm), Mn, Zn, Hg (up to 1383 ppm), and Bi with concentrations of > 1000 ppm. Other trace elements in Fe-tennantite include 100–1000 ppm Ni and Cd, Co and Se concentrations from 10 to 100 ppm, and Ga, In, Sn, Tl, and Pb contents from 1 to 10 ppm. Au concentrations in Fe-tennantite are generally < 1 ppm. Pyrite that is dissolved and replaced by Fe-tennantite is common. Some pyrite occurs in the inner zones of quartz (Fig. 4g). Watanabeite appears as fine anhedral grains filling voids in enargite or Fe-tennantite (Fig. 4a, h). Watanabeite contains 14.69–19.28 wt% As, 5.01–14.51 wt% Sb, up to 4.00 wt% Pb, 9.64 wt% Bi, and 0.44 wt% Ag (Table A2). In addition to Cu sulfosalts as inclusions, dendritic muscovite and euhedral quartz also commonly occur as inclusions in tennantite (Fig. 4f). A few particles of scheelite and fluorapatite are enclosed in enargite and quartz, respectively (Fig. 4g, h). Euhedral quartz hosts droplets of Fe-tennantite rather than enargite and is sometimes eroded by Fe-tennantite (Fig. 4i), indicating that quartz crystallized prior to solidification of Fe-tennantite but after enargite. Carbonate minerals include dominantly Mn-bearing calcite and dolomite as late-stage minerals that cross cut Cu-sulfosalts.

Au-rich veins

Cu–As–Sb–S sulfosalts are the dominant minerals in Au-rich veins; gangue minerals include carbonate and less common euhedral quartz. Enargite and luzonite (high-sulfidation state minerals) were the first minerals to precipitate, followed by tennantite–tetrahedrite, watanabeite, and chalcostibite (intermediate-sulfidation state minerals). The distribution of pyrite, bournonite, galena, native telluride, coloradoite, and Au–Ag tellurides (hessite, petzite, sylvanite, and stützite) is sporadic

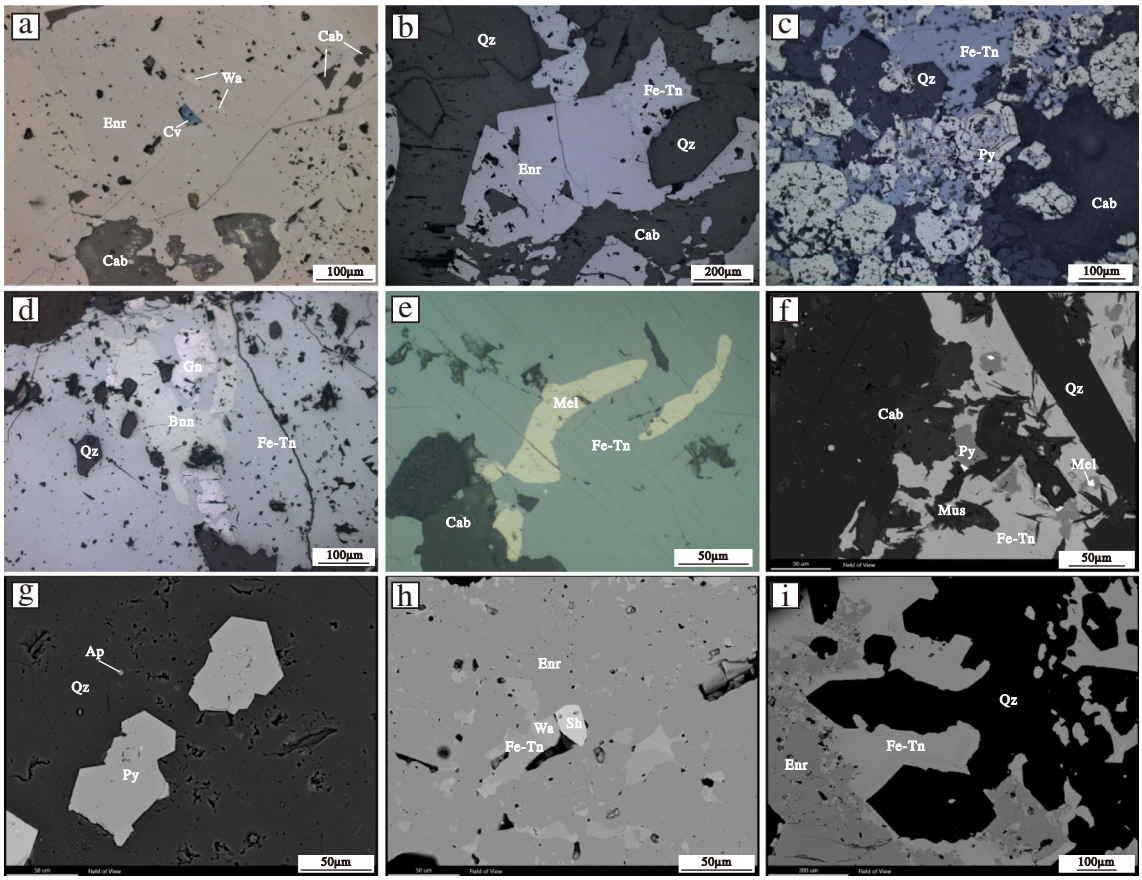

Fig. 4 Photomicrographs (**a**–**e** reflected light; **f**–**i** back-scattered electron (BSE) images) showing paragenetic relationships and associations of minerals from Au-poor veins. **a** Euhedral covellite (Cv), later anhedral watanabeite (Wa), and carbonate minerals (Cab) in enargite (Enr) mass. **b** Euhedral quartz enclosed by enargite, and dimorphic enargite corroded by Fe-tennantite (Fe-Tn) and cut by carbonate veinlets. **c** Early crystalline pyrite (Py) associated with euhedral quartz (Qz), partly replaced by Fe-tennantite along the rim of pyrite. **d** Galena (Gn) and bournonite (Bnn) in Fe-tennantite; **e** Anhedral melonite in Fe-tennantite. **f** Melonite associated with pyrite, dendrite muscovite (Mus), and euhedral quartz in Fe-tennantite. **g** Small fluorapatite (Ap) and euhedral pyrite in the quartz with vugs. **h** Euhedral scheelite (Sh) and intergrown watanabeite and Fe-tennantite in enargite. **i** Enargite replaced by Fe-tennantite, and euhedral quartz hosting droplets of Fe-tennantite enclosed or corroded by Fe-tennantite

(Fig. 5). Enargite contains up to 7.62 wt% Sb, which differs from previous studies that reported no more than 6 wt% Sb contents in enargite from HS epithermal deposits elsewhere (Springer 1969; Pfitzner and Bernert 2004). Enargite also has higher Ge (up to 761 ppm), Sn (up to 379 ppm), and Hg (up to 79.3 ppm) contents compared with enargite in the Au-poor veins (Fig. 3, Table A2). Luzonite, precipitated after enargite, has variable chemical compositions including 5.89–12.73 wt% As and 19.19–8.58 wt% Sb. Luzonite has higher Ge (up to 1188 ppm), W (up to 1168 ppm), Ag (up to 90.7 ppm), and Hg (up to 192 ppm) contents than enargite (Fig. 3b, Table A2). Tennantite–tetrahedrite is spatially associated with watanabeite, and together, they display chemical oscillatory zoning (Fig. 5c, d). Tennantite–tetrahedrite also exhibits Cu-excess and is of a mercurian (Hg up to 5.72 wt%) or ferroan (Fe up to 6.45 wt.%) type (Spiridonov et al. 2005; Table A2). Compared with tennantite in Au-poor veins, tennantite–tetrahedrite in Au-rich veins has higher Sb (12.64–24.89 wt%), Mn, Hg, and Tl (up to 4610 ppm, 5.72 wt%, and 115 ppm, respectively) contents, and lower Co, Ni, Cd, and In contents (Fig. 3b, A1, Tables A2, A4). Watanabeite, analogous to tennantite–tetrahedrite, contains various trace elements, including Fe, Hg (up to 1.10 wt%), Tl (up to 289 ppm), Pb, Bi, Ag (up to 3620 ppm), and Au (up to 79.3 ppm) (Table A2, Fig. 3b, A1). Chalcostibite occurs as euhedral grains that replace tetrahedrite and watanabeite, and it contains up to 0.82 wt% As (Table A2). Hessite, sylvanite, and petzite are always intergrown and occur in watanabeite, tennantite–tetrahedrite, or bournonite, whereas intergrown native Te and stützite occur in tennantite–tetrahedrite, and chalcostibite (Fig. 5d–f).

Discussion

Evidence for HS mineralization

Generally, HS epithermal mineralization is defined by the occurrence of diagnostic minerals (pyrite–enargite/luzonite), acidic hydrothermal alteration (e.g., alunite, kaolinite, and sericite), and anomalously high Cu, As, Sb, S, Au, Ag, Hg, Te, and Bi contents (Arribas et al. 1995; White and Hedenquist 1995; Simmons et al. 2005; Sillitoe 2010). High-grade HS lodes are in all cases closely associated with underlying porphyry intrusions, and characteristic alteration includes a deep near-neutral sericite–pyrite–quartz zone grading upward to relatively shallow quartz–pyrophyllite–alunite zone (Hedenquist et al. 2000; Sillitoe 2010); the Lepanto (Philippines) and El Indio deposits are good examples (Hedenquist et al. 1998; Jannas et al. 1999).

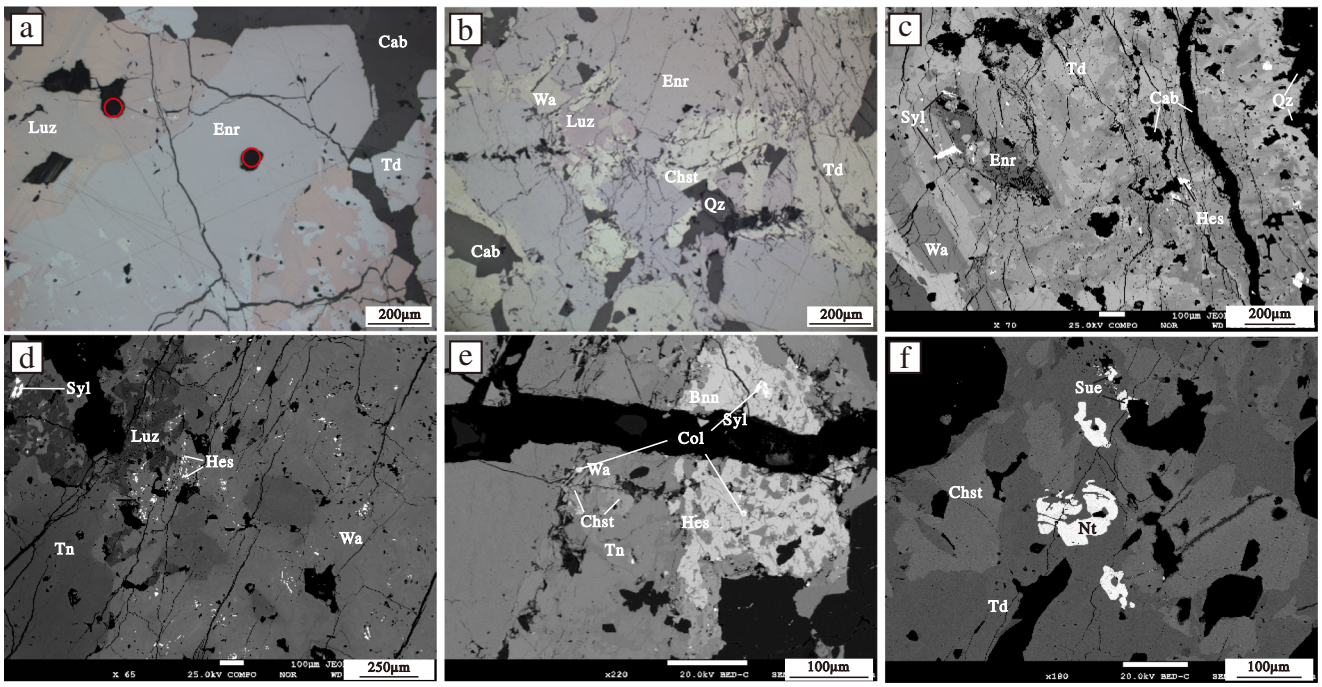

Fig. 5 Photomicrographs (**a**, **b** reflected light; **c**–**f** BSE images) showing representative ore mineral assemblages from Au-rich veins. **a** Early semi-euhedral enargite (Enr) replaced by luzonite (Luz), and tetrahedrite (Td) postdating luzonite cut by carbonite (Cab) veinlets (red circle indicates analysis spot of LA-ICP-MS). **b** Watanabeite (Wa), chalcostibite (Chst), tetrahedrite, and euhedral quartz (Qz) filling open void of early enargite and luzonite. **c** Cu-sulfosalt zone with enargite at the core, outer tetrahedrite and watanabeite (brighter zones are Sb-rich; darker zones are As-rich), with sylvanite and hessite in watanabeite or tetrahedrite. **d** Luzonite replaced by tennantite (Tn), and small grains of hessite and sylvanite in watanabeite. **e** Bournonite (Bnn) and chalcostibite in tennantite and coloradoite (Col) in bournonite and chalcostibite. **f** Native tellurium (Nt) intergrown with stützite (Sue) in chalcostibite and tetrahedrite

The widely distributed massive sulfide veins in the Jiama deposit are inferred to be high-sulfidation (HS) lodes based on the following features: (1) the veins are controlled by steeply dipping fracture arrays and are proximal to the underlying porphyry intrusion; (2) the veins contain diagnostic Cu-sulfosalts, including enargite-luzonite; (3) the coexistence of dendritic muscovite, euhedral quartz, and pyrite in the Cu-sulfosalts may represent weakly acidic formation conditions, similar to the sericite-quartz-pyrite alteration at intermediate depths related to porphyry mineralization; and (4) the ores and major minerals have anomalous Cu, As, Sb, Ag, Hg, Tl, Bi, and Te contents. All four of these characteristics are analogous to those of known HS lodes, such as the El Indio and Chinkuashih (Taiwan) deposits (Mavrogenes et al. 2010; Henley et al. 2012; Henley and Berger 2012). Strongly acidic alunite–vuggy quartz alteration considered to be one of the most important diagnostic features of HS epithermal mineralization has not been observed in veins of the Jiama deposit, most likely because carbonate minerals (pH > 4), which occur ubiquitously in the Jiama deposits, preclude alunite formation (pH < 1). It is also possible that strongly acidic alteration at shallow lithocap depths was subsequently removed by uplift and erosion.

Geochemical evolution

The close proximity of HS veins to porphyry intrusions and their associated pyrite–sericite–quartz alteration indicate a high formation temperature (> 300 °C, Hedenquist and Taran 2013). Normally, arsenic-rich assemblages (enargite–tennantite) precipitate at high temperatures (> 300 °C), and Sb-rich assemblages (luzonite–tetrahedrite–chalcostibite) dominate at relatively low temperatures (Feiss 1974; Luce et al. 1977; Tomkins et al. 2004; Mavrogenes et al. 2010). By this reasoning, the Au-poor veins in the Jiama deposit that are dominated by high-As assemblages imply higher formation temperatures compared with the Au-rich (high Sb assemblage) veins. Temperature influences chemical compositions and structures of enargite–luzonite ($Cu_3(AsSb)S_4$) solid solution. Luzonite is the low-temperature polymorph of enargite, and their inversion temperature is estimated at ~ 280 °C (Poósfai and Buseck 1998; Pfitzner and Bernert 2004). The widespread occurrence of enargite without or rare luzonite in the As-rich, Au-poor veins and coexistence of enargite and luzonite in the Sb–Au-rich veins indicate the precipitation temperatures of Au-poor veins are higher than Au-rich veins. Moreover, the euhedral quartz hosted in tennantite and the occurrence of fluorapatite and scheelite (Fig. 4) in the Au-poor veins also indicate high formation temperatures (> 500 °C, Mavrogenes et al. 2010; Tanner et al. 2015). Based on all of these factors, it is thus inferred that the formation temperatures of Au-poor veins are higher than those of Au-rich veins.

The higher Co and Ni contents of tennantite in higher temperature As-rich, Au-poor veins and higher Hg and Tl contents of tetrahedrite in lower temperature Sb-Au-rich veins (Fig. 3b) suggest that the compositional discrimination between the tennantite–tetrahedrite ($Cu_{12}(AsSb)_4S_{13}$) solid solutions was probably affected by temperature. Mineral trace-element compositions may therefore act as geothermometers. Although Au- and Ag-bearing minerals have a close spatial relationship with enargite or luzonite in some HS epithermal deposits (e.g., the Lepanto deposit), Au- and Ag-bearing minerals generally postdate enargite or luzonite and have intimate association with tennantite–tetrahedrite (Hedenquist et al. 2000). The Au–Ag contents of most intermediate-sulfidation (IS)-state minerals from Jiama (tennantite–tetrahedrite, watanabeite) are several orders of magnitude higher than those of high sulfidation (HS)-state minerals such as enargite and luzonite (Fig. 3b). The higher Ag and Au contents of IS-state minerals (up to 1891 ppm Ag and 2.64 ppm Au in tennantite–tetrahedrite, 3620 ppm Ag and 79.3 ppm Au in watanabeite, or 9.05 ppm Au in chalcostibite) compared with HS-state minerals and presence of Au and Ag minerals (occurring mostly as telluride inclusions in tennantite-tetrahedrite and watanabeite) confirm that the precipitations of Au and Ag are controlled by the solubilities of IS-state minerals (Fig. 3b). The mineral assemblages of Au-poor and Au-rich veins, analogous to El Indio and Chinkuashih, reflect the evolution from As-rich to Sb-rich sulfosalt melts with decreasing temperature (Tomkins et al. 2004; Henley et al. 2012; Henley and Berger 2012). The selective concentration of Au in Sb-rich mineral assemblages (watanabeite–tetrahedrite–chalcostibite) implies that Sb-rich solid solution scavenges gold and controls its precipitation at low temperature. As temperature drops, the solubilities of Au and Ag decrease and exsolution of Au and Ag minerals occurs in IS-state minerals. IS-state minerals (e.g., tennantite–tetrahedrite) also occur extensively in many low- to intermediate-sulfidation Au–Ag deposits worldwide, such as the Victoria deposit (Philippines; Chang et al. 2011) and Emperor deposit (Fiji; Pals and Spry 2003), and may exhibit the same enrichment mechanisms for Au and Ag. We therefore conclude that IS-state minerals or solid solutions control the precipitation of Au and Ag.

Implications of the occurrence of HS veins

Epithermal and porphyry ore deposits are commonly associated with volcanoes, and typically consist of deep porphyry intrusions, intermediate-depth HS lodes, and shallow epithermal lithocap-hosted Cu–Au deposits. In such settings, HS lodes are likely formed in the channel between magma and paleo-fumaroles (Sillitoe and Hedenquist 2003; Scher et al. 2013; Blundy et al. 2015; Nadeau 2015). High-temperature, low-density magmatic vapor released from the magma transports metals and semimetals (e.g., Au, Ag, Cu, As, Sb, Hg, and Tl) via fracture arrays and deposits them into HS veins (Heinrich et al. 1999, 2004; Heinrich 2005; Williams-Jones and Heinrich 2005; Mavrogenes et al. 2010; Berger and Henley 2011; Henley and Berger 2011; Henley et al. 2012).

The Cu-sulfosalt mineral assemblages and enrichment of Cu, Au, Ag As, Sb, Hg, and Tl in HS veins in the Jiama deposit is controlled by fractures. The geologic, mineralogic, and geochemical characteristics are consistent with other global HS lodes. The occurrence of hydrothermal breccia (Fig. 2c) and euhedral quartz–pyrite–sulfosalt assemblages (Fig. 4) in the Jiama HS veins may result from upward expansion of magmatic vapor, a process that has been proposed as playing a critical role in the formation of HS veins in other parts of the world, such as El Indio and Chinkuashih deposit (Mavrogenes et al. 2010; Henley et al. 2012; Henley and Berger 2012). The coexistence of porphyry, skarn, and HS mineralization in the Jiama deposit reflects the evolution of ore-forming fluids and fractionation of metals, characterized by Cu and Mo mineralization in the porphyry; Cu, Au, and Ag mineralization in the proximal skarn; Cu, Pb, and Zn mineralization in the distal skarn; and Cu, As, Sb, Au, Ag, Hg, and Tl enrichment in the HS veins (Fig. 1). High-temperature magmatic brines are likely responsible for porphyry and skarn mineralization, as indicated by the common high-salinity fluid inclusions in quartz in both porphyry and skarn deposits (Zhou et al. 2011). Magmatic vapor generally moves more rapidly over large distances compared with magmatic brine, and therefore skarn and HS mineralization are typically spatially and temporally distinct, with skarn forming later than shallow HS mineralization. However, these relationships are inconsistent with the observation that HS veins cut skarn mineralization in the Jiama deposit. It is possible that skarn mineralization and HS mineralization were controlled by different pulses of high-temperature magmatic fluids derived from deeper magma, resulting in skarn mineralization and relatively later HS mineralization.

The HS veins in the Jiama deposit may represent the root of HS mineralization because they crop out at the surface, suggesting that an upper-lithocap and shallow bulk-tonnage HS epithermal deposits may have been removed by uplift and erosion. The contemporaneous Qulong–Zhibula porphyry–skarn system (~ 15 km southwest of Jiama, Fig. 1a) underwent ≥ 1.8 km of exhumation after mineralization (Zhao et al. 2016; Zhou et al. 2019). Previous studies have suggested that the Gangdese belt has undergone similar rapid uplift and erosion since the Miocene (Copeland et al. 1987, 1995; Fielding 1996; An et al. 2001) leading to extensive exposure of the Gangdese batholith that hosts Miocene porphyry deposits and possible removal of the upper-lithocap and most bulk-tonnage porphyry-related HS epithermal deposits (Hou et al. 2009; Hou et al. 2011; Hou and Zhang 2015). Geological age, formation depth, and upper cover affect the preservation of HS deposits during uplift and erosion (Kesler and Wilkinson 2006). The upper andesite cover in the Duolong ore district played a major role in preserving older Cretaceous epithermal HS mineralization (Li et al. 2015; Song et al. 2017). In the younger Miocene Gangdese belt, volcanic cover is absent. Besides the contribution to the development of skarn in Jiama, impermeable limestone may also play a crucial role for the formation of HS veins by inhibiting upward fluid flow, ground-water recharge, and heat dissipation (Sillitoe et al. 2006). As the shallow bulk-tonnage HS epithermal deposits might be removed by uplift and erosion, we therefore suggest that the HS lode-type deposits should be considered for further prospecting in the Gangdese porphyry belt.

Conclusions

The HS veins in the Jiama deposit comprise predominantly Cu–As–Sb–S sulfosalts and minor tellurides, accompanied by sericite–pyrite–euhedral quartz assemblages. The vein mineralogy and chemistry results suggest a high-sulfidation (HS) environment of formation, and if this conclusion is correct, provides another example of a complete porphyry–skarn–HS system. Magmatic vapor from magmas results in HS vein formation, whereas high-temperature magmatic brine forms porphyry–skarn Cu–Mo–Au–Ag–Pb–Zn mineralization. Based on significantly higher Au and Ag contents in Sb-rich IS-state minerals compared with HS-state minerals in the Jiama deposit, it is evident that IS-state solid solutions controlled the solubilities of Au and Ag. Regional uplift and erosion caused the absence of subsurface bulk-tonnage HS epithermal deposits in the Gangdese porphyry belt. However, high-grade HS lodes near the porphyry deposits at depth should be given more attention for exploration.

Acknowledgments We thank Chuyi Lan from Huatailong Mining Development Co., Ltd for providing field and geological support. We gratefully acknowledge Zhaoshan Chang, Chusi Li, Wei Mao, Jingjing Zhu, Langzhang Xing and Xingchun Zhang for fruitful discussions, as well as Wenlan Zhang from Nanjing University for help with EPMA analysis and Zhihui Dai for LA–ICP–MS analyses. Profs. John Mavrogenes (reviewer) and Karen Kelley (Associate Editor) are appreciated for scientific suggestions and extensive editing of the manuscript, and Prof. Bernard Lehmann (Editor) for handling the manuscript.

Funding information This study was supported by the National Natural Science Foundation of China (41425011) and the Second Tibetan Plateau Scientific Expedition and Research (STEP) (2019QZKK0806).

References

An ZS, Kutzbach JE, Prell WL, Porter SC (2001) Evolution of Asian monsoons and phased uplift of the Himalaya-Tibetan plateau since Late Miocene times. Nature 411:62

Arribas A Jr, Hedenquist JW, Itaya T, Okada T, Concepción RA, Garcia JS Jr (1995) Contemporaneous formation of adjacent porphyry and epithermal Cu-Au deposits over 300 ka in Northern Luzon, Philippines. Geology 23:337–340

Berger BR, Henley RW (2011) Magmatic-vapor expansion and the formation of high-sulfidation gold deposits: structural controls on hydrothermal alteration and ore mineralization. Ore Geol Rev 39:75–90

Bissig T, Clark AH, Lee JK, Hodgson CJ (2002) Miocene landscape evolution and geomorphologic controls on epithermal processes in the El Indio-Pascua Au-Ag-Cu belt, Chile and Argentina. Econ Geol 97:971–996

Bissig T, Clark AH, Rainbow A, Montgomery A (2015) Physiographic and tectonic settings of high-sulfidation epithermal gold–silver deposits of the Andes and their controls on mineralizing processes. Ore Geol Rev 65:327–364

Blundy J, Mavrogenes J, Tattitch B, Sparks S, Gilmer A (2015) Generation of porphyry copper deposits by gas–brine reaction in volcanic arcs. Nat Geosci 8:235

Chambefort I, Moritz R, von Quadt A (2007) Petrology, geochemistry and U–Pb geochronology of magmatic rocks from the high-sulfidation epithermal Au–Cu Chelopech deposit, Srednogorie zone, Bulgaria. Mineral Deposita 42:665–690

Chang ZS, Hedenquist JW, White NC, Cooke DR, Roach M, Deyell CL, Garcia J, Gemmell JB, McKnight S, Cuison AL (2011) Exploration tools for linked porphyry and epithermal deposits: example from the Mankayan intrusion-centered Cu-Au district, Luzon, Philippines. Econ Geol 106:1365–1398

Chiaradia M (2014) Copper enrichment in arc magmas controlled by overriding plate thickness. Nat Geosci 7:43–46

Copeland P, Harrison TM, Wea K, Ronghua X, Yuquan Z (1987) Rapid early Miocene acceleration of uplift in the Gangdese Belt, Xizang (Southern Tibet), and its bearing on accommodation mechanisms of the India-Asia collision. Earth Planet Sci Lett 86:240–252

Copeland P, Harrison TM, Pan Y, Kidd W, Roden M, Zhang Y (1995) Thermal evolution of the Gangdese batholith, Southern Tibet: a history of episodic unroofing. Tectonics 14:223–236

Danyushevsky L, Robinson P, Gilbert S, Norman M, Large R, McGoldrick P, Shelley M (2011) Routine quantitative multi-element analysis of sulphide minerals by laser ablation ICP-MS: standard development and consideration of matrix effects. Geochemistry: Exploration, Environment, Analysis 11:51–60

Feiss PG (1974) Reconnaissance of the tetrahedrite-tennantite/enargite-famatinite phase relations as a possible geothermometer. Econ Geol 69:383–390

Fielding EJ (1996) Tibet uplift and erosion. Tectonophysics 260:55–84

Hedenquist JW, Taran YA (2013) Modeling the formation of advanced argillic lithocaps: volcanic vapor condensation above porphyry intrusions. Econ Geol 108:1523–1540

Hedenquist JW, Arribas A, Reynolds TJ (1998) Evolution of an intrusion-centered hydrothermal system: Far Southeast-Lepanto porphyry and epithermal Cu-Au deposits, Philippines. Econ Geol 93:373–404

Hedenquist JW, Arribas A, Gonzalez-Urien E (2000) Exploration for epithermal gold deposits. Rev Econ Geol 13:45–77

Heinrich CA (2005) The physical and chemical evolution of low-salinity magmatic fluids at the porphyry to epithermal transition: a thermodynamic study. Mineral Deposita 39:864–889

Heinrich CA, Gunther D, Audétat A, Ulrich T, Frischknecht R (1999) Metal fractionation between magmatic brine and vapor, determined by microanalysis of fluid inclusions. Geology 27:755–758

Heinrich CA, Driesner T, Stefánsson A, Seward TM (2004) Magmatic vapor contraction and the transport of gold from the porphyry environment to epithermal ore deposits. Geology 32:761–764

Henley RW, Berger BR (2011) Magmatic-vapor expansion and the formation of high-sulfidation gold deposits: chemical controls on alteration and mineralization. Ore Geol Rev 39:63–74

Henley RW, Berger BR (2012) Pyrite–sulfosalt reactions and semimetal fractionation in the Chinkuashih, Taiwan, copper–gold deposit: a 1 Ma paleo-fumarole. Geofluids 12:245–260

Henley RW, Mavrogenes J, Tanner D (2012) Sulfosalt melts and heavy metal (As-Sb-Bi-Sn-Pb-Tl) fractionation during volcanic gas expansion: the El Indio (Chile) paleo-fumarole. Geofluids 12:199–215. https://doi.org/10.1111/j.1468-8123.2011.00357.x

Hou ZQ (2010) Metallogensis of continental collision. Acta Geol Sin 84: 30–58

Hou ZQ, Zhang HR (2015) Geodynamics and metallogeny of the eastern Tethyan metallogenic domain. Ore Geol Rev 70:346–384

Hou ZQ, Yang ZM, Qu XM, Meng XJ, Li ZQ, Beaudoin G, Rui ZY, Gao YF, Zaw K (2009) The Miocene Gangdese porphyry copper belt generated during post-collisional extension in the Tibetan Orogen. Ore Geol Rev 36:25–51

Hou ZQ, Zhang HR, Pan XF, Yang ZM (2011) Porphyry Cu (–Mo–Au) deposits related to melting of thickened mafic lower crust: examples from the eastern Tethyan metallogenic domain. Ore Geol Rev 39: 21–45

Hu YB, Liu JQ, Ling MM, Ding W, Liu Y, Zartman RE, Ma XF, Liu DY, Zhang CC, Sun SJ (2015) The formation of Qulong adakites and their relationship with porphyry copper deposit: geochemical constraints. Lithos 220:60–80

Jannas RR, Beane RE, Ahler BA, Brosnahan DR (1990) Gold and copper mineralization at the El Indio deposit, Chile. J Geochem Explor 36: 233–266

Jannas R, Bowers T, Petersen U, Beane R (1999) High-sulfidation deposit types in the El Indio district, Chile. Soc Econ Geol Spec Publ 7:219–266

Kesler SE, Wilkinson BH (2006) The role of exhumation in the temporal distribution of ore deposits. Econ Geol 101:919–922

Lee C-TA (2014) Economic geology: copper conundrums. Nat Geosci 7: 10–11

Li GM, Zhang X-N, Qin K-Z, Sun X-G, Zhao J-X, Yin X-B, Jinxiang L-I, Yuan H-S (2015) The telescoped porphyry-high sulfidation epithermal Cu(-Au) mineralization of Rongna deposit in Duolong ore cluster at the southern margin of Qiangtang Terrane,Central Tibet:integrated evidence from geology,hydrothermal alteration and sulfide assemblages. Acta Petrol Sin 31:2307–2324

Li HF, Tang JX, Hu GY, Ding S, Li Z, Xie FW, Teng L, Cui SY (2019) Fluid inclusions, isotopic characteristics and geochronology of the Sinongduo epithermal Ag-Pb-Zn deposit, Tibet, China. Ore Geol Rev 107:692–706

Longerich H, Sylvester P (2008) Laser ablation ICP-MS in the earth sciences: current practices and outstanding issues

Luce FD, Tuttle CL, Skinner B (1977) Studies of sulfosalts of copper; V, phases and phase relations in the system Cu-Sb-As-S between 350 degrees and 500 degrees C. Econ Geol 72:271–289

Marcoux E, Milési J, Moëlo Y (1994) Vinciennite and Cu-excess tennantite from the Layo (Cu, Sn, As, Au) epithermal deposit (Southern Peru). Mineral Petrol 51:21–36

Mavrogenes J, Henley RW, Reyes AG, Berger B (2010) Sulfosalt melts: evidence of high-temperature vapor transport of metals in the formation of high-sulfidation lode gold deposits. Econ Geol 105:257–262

Meinert LD (2000) Gold in skarns related to epizonal intrusions. Rev Econ Geol 13:347–375

Meinert LD, Dipple GM, Nicolescu S (2005) World skarn deposits. Econ Geol 100:299–336

Molnár F, Jung P, Kupi L, Pogány A, Vágó E, Viktorik O, Pécskay Z, Hurai V (2008) Epithermal zones of the porphyry-skarn-epithermal ore complex at Recsk. â Recsk and LahÃ³ca Geology of the Paleogene ore complexâ 73:99–128

Muntean JL, Einaudi MT (2001) Porphyry-epithermal transition: Maricunga belt, Northern Chile. Econ Geol 96:743–772

Nadeau O (2015) Economic geology: ore metals beneath volcanoes. Nat Geosci 8:168

Pals D, Spry P (2003) Telluride mineralogy of the low-sulfidation epithermal Emperor gold deposit, Vatukoula, Fiji. Mineral Petrol 79:285–307

Pfitzner A, Bernert T (2004) The system Cu3AsS4–Cu3SbS4 and investigations on normal tetrahedral structures. Zeitschrift für Kristallographie-Crystalline Materials 219:20–26

Poósfai M, Buseck PR (1998) Relationships between microstructure and composition in enargite and luzonite. Am Mineral 83:373–382
Qu XM (2001) Is Gangdese porphyry copper belt the second "Yulong" copper belt? 20:355-366
Qu XM, Hou ZQ, Li YG (2004) Melt components derived from a subducted slab in late orogenic ore-bearing porphyries in the Gangdese copper belt, Southern Tibetan Plateau. Lithos 74:131–148
Ren YS, Su DK, Zhang JS (2002) Superimposted mineralization of gold in Jiama copper polymentallic deposit. J Jilin Univ (Earth Sci Ed) 32:225–228
Repstock A, Voudouris P, Kolitsch U (2015) New occurrences of watanabeite, colusite,"arsenosulvanite" and "Cu-excess" tetrahedrite-tennantite at the Pefka high-sulfidation epithermal deposit, northeastern Greece. Neues Jahrbuch für Mineralogie-Abhandlungen: Journal of Mineralogy and Geochemistry 192: 135–149
Richards JP (2015) Tectonic, magmatic, and metallogenic evolution of the Tethyan orogen: from subduction to collision. Ore Geol Rev 70: 323–345
Scher S, Williams-Jones A, Williams-Jones G (2013) Fumarolic activity, acid-sulfate alteration, and high sulfidation epithermal precious metal mineralization in the crater of Kawah Ijen volcano, Java, Indonesia. Econ Geol 108:1099–1118
Sillitoe RH (2010) Porphyry copper systems. Econ Geol 105:3–41
Sillitoe RH, Hedenquist JW (2003) Linkages between volcanotectonic settings, ore-fluid compositions, and epithermal precious metal deposits. Special Publication-Society of Economic Geologists 10:315–343
Sillitoe RH, Perelló J (2005) Andean copper province: tectonomagmatic settings, deposit types, metallogeny, exploration, and discovery. Economic Geology 100th anniversary volume:845–890
Sillitoe RH, Hall DJ, Redwood SD, Waddell AH (2006) Pueblo Viejo high-sulfidation epithermal gold-silver deposit, Dominican Republic: a new model of formation beneath barren limestone cover. Econ Geol 101:1427–1435
Simmons SF, White NC, John DA (2005) Geological characteristics of epithermal precious and base metal deposits. Economic Geology 100th anniversary volume 29:485–522
Song Y, Yang HH, Lin B, Liu ZB, Qin W, Ke G, Chao Y, Xiang F (2017) The preservation system of epithermal deposits in South Qiangtang terrane of central Tibetan Plateau and its significance: a case study of the Tiegelongnan superlarge deposit. Acta Geosci Sin 38:659–669
Spiridonov E, Maleev M, Kovachev V, Kulikova I, Nazmova G, Filimonov S (2005) Minerals of fahlore group: indicators of ore genesis Proc Jubilee Intern Conf Bulg Geol Soc 80th Ann. pp 79–82
Springer G (1969) Compositional variations in enargite and luzonite. Mineral Deposita 4:72–74
Sun WD, Wang JT, Zhang LP, Zhang CC, Li H, Ling MX, Ding X, Li CY, Liang HY (2017) The formation of porphyry copper deposits. Acta Geochimica 36:9–15
Sun XL, Sun WD, Hu YD, Ding W, Ireland T, Zhan MZ, Liu JQ, Ling MX, Ding X, Zhang ZF (2018) Major Miocene geological events in Southern Tibet and Eastern Asia induced by the subduction of the Ninetyeast ridge. Acta Geochimica 37:395–401
Takács À, Molnár F, Turi J, Mogessie A, Menzies JC (2017) Ore mineralogy and fluid inclusion constraints on the temporal and spatial evolution of a high-sulfidation epithermal Cu-Au-Ag deposit in the Recsk ore complex, Hungary. Econ Geol 112:1461–1781
Tang JX, Wang DH, Wang XW, Zhong KH, Ying LJ, Zheng WB, Li FJ, Guo N, Qin ZP (2010) Geological features and metallogenic model of the Jiama copper-polymetallic deposit in Tibet. Diqiu Xuebao(Acta Geoscientica Sinica) 31:495–506
Tang JX, Deng SL, Zheng WB, Ying LJ, Wang XW, Zhong KH, Qin ZP, Ding F, Li FJ, Tang X (2011) An exploration model for Jiama copper polymetallic deposit in Maizhokunggar County, Tibet. Mineral Deposits 30:179–196
Tang JX, Zheng WB, Cheng YC, Wang DH, Ying LJ, Qin ZP (2013) Prospecting breakthrough of the deep porphyry ore body and its significance in Jiama copper polymetallic deposit, Tibet. China Journal of Jilin University (Earth Science Edition) 43:1100–1110
Tang JX, Sun XG, Ding S, Wang Q, Wang YY, Yang C, Chen HQ, Li YB, Wei LJ (2014) Discovery of the epithermal deposit of Cu (Au-Ag) in the Duolong ore concentrating area, Tibet. Acta Geosci Sin 35:6–10
Tanner D, Henley RW, Mavrogenes JA, Holden P, Mernagh TP (2015) Silica hydrate preserved with δ^{18}O-rich quartz in high-temperature hydrothermal quartz in the high sulfidation copper-gold deposit at El Indio, Chile. Chem Geol 391:90–99
Taylor BE (2007) Epithermal gold deposits. Mineral deposits of Canada: a synthesis of major deposit-types, district metallogeny, the evolution of geological provinces, and exploration methods Edited by WD Goodfellow Geological Association of Canada, Mineral Deposits Division, Special Publication 5:113–139
Tomkins AG, Pattison DR, Zaleski E (2004) The Hemlo gold deposit, Ontario: an example of melting and mobilization of a precious metal-sulfosalt assemblage during amphibolite facies metamorphism and deformation. Econ Geol 99:1063–1084
Voudouris PC, Melfos V, Spry PG, Moritz R, Papavassiliou C, Falalakis G (2011) Mineralogy and geochemical environment of formation of the Perama Hill high-sulfidation epithermal Au-Ag-Te-Se deposit, Petrota Graben, NE Greece. Mineralogy & Petrology 103:79–100
Wang WP, Tang JX (2011) Rock types and genetic significance of hornfels and location prediction of concealed porphyry bodies in Jiama copper polymetallic deposit, Tibet. Mineral Deposits 30:1017–1036
Wang DH, Tang JX, Ying LJ, Lin B, Ding S (2011) Hornfels feature in the Jiama ore deposit, Tibet and its significance on deep prospecting. Acta Petrol Sin 27:2103–2108
Wang R, Richards JP, Hou ZQ, Yang ZM, DuFrane SA (2014) Increased magmatic water content—the key to Oligo-Miocene porphyry Cu-Mo±Au formation in the eastern Gangdese Belt, Tibet. Econ Geol 109:1315–1339
White NC, Hedenquist JW (1995) Epithermal gold deposits: styles, characteristics and exploration. SEG newsletter 23:9–13
Williams-Jones AE, Heinrich CA (2005) 100th anniversary special paper: vapor transport of metals and the formation of magmatic-hydrothermal ore deposits. Econ Geol 100:1287–1312
Zhao JX, Qin KZ, Xiao B, McInnes B, Li GM, Evans N, Cao MJ, Li JX (2016) Thermal history of the giant Qulong Cu–Mo deposit, Gangdese metallogenic belt, Tibet: constraints on magmatic–hydrothermal evolution and exhumation. Gondwana research 36: 390-409. Doi: https://doi.org/10.1016/j.gr.2015.07.005
Zheng WB, Tang JX, Zhong KH, Ying LJ, Leng QF, Ding S, Lin B (2016) Geology of the Jiama porphyry copper–polymetallic system, Lhasa Region, China. Ore Geology Reviews 74:151–169. doi: https://doi.org/10.1016/j.oregeorev.2015.11.024
Zhou Y, Wang XW, Tang JX, Qin ZP, Peng HJ, Li AG, Yang K, Wang H, Li J, Zhang JC (2011) Origin and evolution of ore-forming fluids from Jiama copper polymetallic deposit in Tibet. Mineral Deposits 30:231–248
Zhou A, Dai J-G, Li Y-L, Li H-A, Tang J-X, Wang C-S (2019) Differential exhumation histories between Qulong and Xiongcun porphyry copper deposits in the Gangdese copper metallogenic belt: insights from low temperature thermochronology. Ore Geol Rev